

This is an Open Access document downloaded from ORCA, Cardiff University's institutional repository:<https://orca.cardiff.ac.uk/id/eprint/150424/>

This is the author's version of a work that was submitted to / accepted for publication.

Citation for final published version:

Wu, Tianchi, Cai, Guoqing, Cleall, Peter and Tripathy, Snehasis 2022. Microstructurally related model for predicting behaviour of unsaturated soils with double porosity in triaxial space. *International Journal of Geomechanics* 22 (12)

Publishers page: [http://dx.doi.org/10.1061/\(ASCE\)GM.1943-5622.00025...](http://dx.doi.org/10.1061/(ASCE)GM.1943-5622.00025...)

Please note:

Changes made as a result of publishing processes such as copy-editing, formatting and page numbers may not be reflected in this version. For the definitive version of this publication, please refer to the published source. You are advised to consult the publisher's version if you wish to cite this paper.

This version is being made available in accordance with publisher policies. See <http://orca.cf.ac.uk/policies.html> for usage policies. Copyright and moral rights for publications made available in ORCA are retained by the copyright holders.



1           **Microstructurally related model for predicting**  
2 **behaviour of unsaturated soils with double porosity in**  
3           **triaxial space**

4           Tianchi Wu<sup>1</sup>, Guoqing Cai<sup>2</sup>, Peter Cleall<sup>3</sup>, Snehasis Tripathy<sup>4</sup>

5           <sup>1</sup>Ph.D. student, School of Engineering, Cardiff University, Cardiff, United Kingdom

6           <sup>2</sup>Professor, School of Civil Engineering, Beijing Jiaotong University, Beijing, China.

7           Corresponding author Email: guoqing.cai@bjtu.edu.cn

8           <sup>3</sup>Professor, School of Engineering, Cardiff University, Cardiff, United Kingdom.

9           <sup>4</sup>Professor, School of Engineering, Cardiff University, Cardiff, United Kingdom.

10  
11 **ABSTRACT**

12           Microstructure can have an important impact on the hydraulic and mechanical  
13 behaviour of unsaturated soil and so it is necessary for it to be considered in constitutive  
14 models to enable accurate predictions of soil behaviour. This paper focuses on  
15 constitutive modelling of soils exhibiting a dual-porosity structure. Based on the  
16 assumption that macro and micropores contained in the double porosity structure have  
17 different influences on the mechanical and hydraulic behaviour, the effective degree of  
18 saturation was selected as a microstructural index. This microstructural index was  
19 implemented within a Bishop's effective stress based approach and the Glasgow  
20 Coupled Model and the Modified Camclay Model were adopted as the basic framework  
21 for the development of a constitutive model. Typical samples of low-expansive, non-  
22 expansive and collapsible soils with dual porosity were selected to validate the model's

23 performance, with the model found to perform well when compared with experimental  
24 data in terms of isotropic compression, triaxial shear and wetting tests.

25 **Key words:** unsaturated soils; coupled constitutive model; effective degree of saturation;  
26 microstructure

## 27 **INTRODUCTION**

28 Recently, there has been growing interest in how the microstructure affects the  
29 hydraulic and mechanical behaviour of unsaturated soils (Cai et al. 2014, 2020b; a;  
30 Cuisinier et al. 2011; Jia et al. 2020; Low et al. 2008; Manahiloh et al. 2016;  
31 Ranaivomanana et al. 2017; Romero and Simms 2008; Sánchez et al. 2016; Sergeev  
32 et al. 1980; Tian-er and Lin 2010; Trzeciński and Wójcik 2019). The microstructure can  
33 be classified as having single or double porosity (Alazaiza et al. 2017; Bagherieh et al.  
34 2009; Russell 2010) according to features of pore size distribution (PSD). The PSD for  
35 double porosity manifests significant bimodality, which is related to the presence of  
36 both macro and micropores (Casini et al. 2012; Lewandowska et al. 2004; Musso et al.  
37 2014; Ngien et al. 2012). According to Li et al (2019), the macropores are mainly  
38 deformed during loading while the micropores are less affected; however, during drying  
39 and wetting process, the micropores will exhibit significant changes and be  
40 accompanied by reversible volumetric deformation.

41 A review of the literature (Cai et al. 2018; Li et al. 2013, 2019; Mašín 2013; Mašín  
42 et al. 2005) suggests that there are two ways to consider the effects of double porosity  
43 on the hydraulic and mechanical behaviour of unsaturated soils. The first way is

44 adopting a specific microstructural index to represent the main features of double  
45 porosity. For example, the effective degree of saturation can be adopted as this index  
46 considers the different impacts of water within macropores and micropores, which  
47 provides an indirect way to take features of double porosity into consideration.  
48 Adopting this approach, Cai et al. (2018) established a hydro-mechanical coupled  
49 constitutive model based on the Glasgow Coupled Model that was validated against  
50 isotropic compression tests of double-porosity soils. Li et al. (2019) also used the  
51 effective degree of saturation to establish a model for unsaturated soils with double  
52 porosity. Their model used average effective stress, deviator stress and modified suction  
53 as the main stress variables. However, the model established by Cai et al (2018) is  
54 limited to isotropic loading and so cannot consider shear response. Also whilst the  
55 model established by Li et al. (2019) can consider shear response it adopts average  
56 effective stress as one of the main stress variables and so cannot consider how the three  
57 principal stresses will change respectively in a triaxial space, such as during shear at a  
58 constant net mean stress. A second way is to establish mutually independent models for  
59 the loading behaviour of macropores and micropores. For example, Mašin (2013) used  
60 different constitutive models for the behaviour of macropores and micropores and  
61 satisfactorily reproduced macro-mechanical properties by establishing a corresponding  
62 coupling relationship. However, this model has a complex form and requires  
63 determination of numerous material parameters, which limits its practical application.

64 This paper introduces a microstructurally based constitutive model for unsaturated

65 soils with double porosity. The key contribution is that the model adopts effective  
66 degree of saturation as the microstructural index and uses the Glasgow Coupled Model  
67 as the basic framework to acquire a concise constitutive relationship, which needs only  
68 nine physically meaningful parameters. The generalized tensor and Modified Camclay  
69 Model (Roscoe and Burland 1968) were adopted to extend the model to a three-  
70 dimensional space where both isotropic compression and shear loading can be  
71 simulated. The model is validated through experimental results of low-expansive  
72 Speswhite kaolin (Sivakumar 1993), low-plastic clay (Almahbobi 2018) and non-  
73 expansive Jossigny silt (Cui and Delage 1996) in terms of wetting, saturated and  
74 unsaturated, isotropic compression and shear tests.

## 75 **CONSTITUTIVE MODEL**

76 The effective degree of saturation was adopted to consider the effects of double  
77 porosity on the mechanical and hydraulic behaviour of unsaturated soils. The model  
78 was established based on the framework of the Glasgow Coupled Model (GCM)  
79 (Wheeler et al. 2003). The GCM is an important constitutive model which considers  
80 the impact of degree of saturation on effective stress and behaviour of unsaturated soils.  
81 Unlike other models which adopt a single loading-collapse yield curve in the net mean  
82 stress-suction plane to study the elasto-plastic mechanism during suction decrease or  
83 mechanical loading, the GCM utilises yield curves in the effective stress-modified  
84 suction plane (see **Fig. 1**). These yield curves are: the loading-collapse line (LC), which  
85 serves as the boundary between elastic volumetric change and plastic volumetric

86 change when the effective stress increases or decrease; the suction-decrease line (SD),  
87 which acts as the boundary between elastic and plastic changes of degree of saturation  
88 when suction decreases; and the suction-increase line (SI) which is defined to represent  
89 the position where plastic change of degree of saturation will occur during suction  
90 increase. According to Lloret-Cabot et al. (2013), the generalized stress tensor was  
91 adopted to study both mechanical and hydraulic in a unified framework and Modified  
92 Camclay Model (Roscoe and Burland 1968) was adopted to extend the model to a three-  
93 dimensional space to study the shear behaviour of soils.

#### 94 **Effective Degree of Saturation**

95 According to Alonso et al. (2010), pores within double-porosity soils can be  
96 grouped into two categories: macropores partially filled with freely available water (the  
97 main source of suction) and micropores filled with bound water. Correspondingly,  
98 degree of saturation  $S_r$  can also be separated into two components: macroscopic degree  
99 of saturation  $S_r^M$ , which contributes to the mechanical behaviour of soils, and  
100 microscopic degree of saturation  $S_r^m$ , which is considered constant and independent of  
101 applied suction and load ( $S_r = S_r^m + S_r^M$ ). Subsequently the effective degree of  
102 saturation can be defined as:

$$103 \quad S_e = \frac{S_r - S_r^m}{1 - S_r^m} \quad (1)$$

104 with this definition, effective degree of saturation is a microstructurally based variable,  
105 which considers the feature of double porosity and establishes a link between this

106 structure and the hydro-mechanical behaviour of soils. The effective degree of  
 107 saturation can be represented by the residual degree of saturation because it is related  
 108 to water stored within small occluded pores or intercrystalline pore space, where  
 109 physico-chemical bonds hold the water to the solid and are not strongly related to  
 110 applied suction or mechanical load, resulting in a very limited impact on effective stress  
 111 (Alonso et al. 2010).

## 112 **Stress Variables**

113 According to Houlsby's theory (Houlsby 1997), the increment of work input  $dW$   
 114 per unit volume of unsaturated soil can be written as:

$$115 \quad dW = [\sigma_{ij} - (S_r u_w + (1 - S_r) u_a) \delta_{ij}] d\varepsilon_{ij} - (u_a - u_w) n dS_r \quad (2)$$

116 where  $\sigma_{ij}$  is the stress tensor,  $d\varepsilon_{ij}$  is the strain increment tensor,  $\delta_{ij}$  is the Kronecker  
 117 delta,  $u_w$  is the water pressure,  $u_a$  is the air pressure,  $S_r$  is the degree of saturation and  
 118  $n$  is the porosity.

119 Incorporating the Bishop's effective stress (Bishop 1959) and the effective degree  
 120 of saturation  $S_e$  into (2), the expression of the Bishop's stress tensor  $\sigma_{ij}^*$  and the  
 121 modified suction  $s^*$  can be derived as:

$$122 \quad \sigma_{ij}^* = \sigma_{ij} - (S_e u_w + (1 - S_e) u_a) \delta_{ij} \quad (3)$$

$$123 \quad s^* = (u_a - u_w) n \quad (4)$$

124 Correspondingly, the stress and strain increment vectors have been adopted as  
 125 follows:

126 
$$\mathbf{d}\boldsymbol{\sigma}^* = (d\sigma_{xx}^*, d\sigma_{yy}^*, d\sigma_{zz}^*, d\sigma_{xy}^*, d\sigma_{yz}^*, d\sigma_{xz}^*)^T \quad (5)$$

127 
$$\mathbf{d}\boldsymbol{\varepsilon} = (d\varepsilon_{xx}, d\varepsilon_{yy}, d\varepsilon_{zz}, d\varepsilon_{xy}, d\varepsilon_{yz}, d\varepsilon_{xz})^T \quad (6)$$

128 Following the approach of Lloret-Cabot et al. (2013) and taking the modified  
 129 suction  $s^*$  and effective degree of saturation  $S_e$  as generalized stress and strain  
 130 invariants, then the generalized stress and strain increment vectors can be written as:

131 
$$\mathbf{d}\boldsymbol{\sigma}^* = (d\sigma_{xx}^*, d\sigma_{yy}^*, d\sigma_{zz}^*, d\sigma_{xy}^*, d\sigma_{yz}^*, d\sigma_{xz}^*, ds^*)^T \quad (7)$$

132 
$$\mathbf{d}\tilde{\boldsymbol{\varepsilon}} = (d\varepsilon_{xx}, d\varepsilon_{yy}, d\varepsilon_{zz}, d\varepsilon_{xy}, d\varepsilon_{yz}, d\varepsilon_{xz}, -dS_e)^T \quad (8)$$

133 For a hydro-mechanical coupled model, the increment of stress is the collective  
 134 output of the force, suction and effective degree of saturation. According to (3) and (4),  
 135 the formulas for the increments of generalized stress can be defined as:

136 
$$d\sigma_{ij}^* = d(\sigma_{ij} - u_a \delta_{ij}) + (sdS_e + S_e ds) \delta_{ij} \quad (9)$$

137 
$$ds^* = nds - \frac{sd\varepsilon_v}{v} \quad (10)$$

138 where  $s = u_a - u_w$  is the suction,  $v$  is the specific volume and  $d\varepsilon_v$  is the increment of  
 139 volumetric strain.

## 140 Yield Surfaces

141 Three yield surfaces, including the loading-collapse surface (LC), suction increase  
 142 surface (SI) and suction decrease surface (SD) were adopted based on Lloret-Cabot et  
 143 al., (2013), as seen in **Fig. 1**, in the  $q: p^*: s^*$  stress space (where  $q$  is the deviatoric stress,  
 144  $p^*$  is the mean Bishop's stress). The Modified CamClay Model (MCC), with a unique  
 145  $M$  (assuming that a unique Critical State Line in the  $q: p^*$  plane exists), was adopted as  
 146 the reference model for the saturated condition. Then the algebraic expressions of the



147 three yield surfaces are given as follows:

$$148 \quad F_{LC} = q^2 - M^2 p^* (p_0^* - p^*) = 0 \quad (11)$$

$$149 \quad F_{SI} = s^* - s_I^* = 0 \quad (12)$$

$$150 \quad F_{SD} = s_D^* - s^* = 0 \quad (13)$$

151 where  $p_0^*$  is the Bishop's pre-consolidation pressure which defines the position of  $F_{LC}$ ,

152  $s_I^*$  and  $s_D^*$  are the modified suctions that locate  $F_{SI}$  and  $F_{SD}$ , respectively.

### 153 **Coupling between Yield Surfaces**

154 Yielding on either of the three surfaces will lead to the movement of the other two  
155 surfaces. The plastic mechanisms and couplings of yield surfaces are defined as follows:

156 1) yielding on the LC yield surface ( $F_{LC}$ ) will bring about plastic volumetric strain  
157 with no irreversible change of the effective degree of saturation  $S_e$ , which in turn  
158 triggers upward movements of the SI and SD surfaces. This coupling is established,  
159 with a coupling parameter  $k_2$ , by:

$$160 \quad \frac{ds_I^*}{s_I^*} = \frac{ds_D^*}{s_D^*} = k_2 \frac{dp_0^*}{p_0^*} \quad (14)$$

161 2) yielding on the SI/SD yield surfaces ( $F_{SI} / F_{SD}$ ) will lead to a plastic reduction of  
162  $S_e$  but no change of plastic volumetric strain, which in turn induces upward/downward  
163 movement of the SD/SI surfaces and outward/inward movement of the LC surface.

164 This coupling is established, with a coupling parameter  $k_1$ , by:

$$165 \quad \frac{dp_0^*}{p_0^*} = k_1 \frac{ds_I^*}{s_I^*} = k_1 \frac{ds_D^*}{s_D^*} \quad (15)$$

## 166 Flow Rules

167 Flow rules define the orientation of the generalized plastic strain increments during  
168 yielding. This paper assumes associated flow rules and adopts the generalized  
169 expression presented by Lloret Cabot et al., ( 2013) :

$$170 \quad d\tilde{\boldsymbol{\varepsilon}}_j^p = d\lambda_l^j \frac{\partial F_l}{\partial \boldsymbol{\sigma}} \quad \text{with } l = \text{LC}, \beta; j = \text{LC}, \beta, \text{LC} + \beta; \beta = \text{SI or SD} \quad (16)$$

171 where  $d\lambda_l^j$  is the plastic multiplier with  $j$  related to the plastic mechanism which is  
172 active (e.g. when yield on LC yield surface is activated  $j$  is LC and for yield on SI or  
173 SD  $j$  is LC is  $\beta$ ) and  $l$  is associated with plastic changes of effective degrees of  
174 saturation (when  $l$  is  $\beta$ ) or volumetric strains (when  $l$  is LC).

## 175 Hardening Laws

176 The generalized hardening laws determining the relationships between increments  
177 of plastic volumetric strain  $d\varepsilon_v^p$ , increments of the plastic effective degree of saturation  
178  $dS_e^p$ , and increments of the hardening variables  $dp_o^*$ ,  $ds_1^*$ ,  $ds_D^*$  are as follows:

$$179 \quad dp_o^* = p_o^* \left[ \frac{vd\varepsilon_v^p}{\lambda - \kappa} - \frac{k_1 dS_e^p}{\lambda_s - \kappa_s} \right] \quad (17)$$

$$180 \quad ds_{1/D}^* = s_{1/D}^* \left[ -\frac{dS_e^p}{\lambda_s - \kappa_s} + k_2 \frac{vd\varepsilon_v^p}{\lambda - \kappa} \right] \quad (18)$$

## 181 Generalized Stress-Strain Relationship

182 Current knowledge on the elasto-plastic mechanisms of unsaturated soils indicates  
183 that the generalized strains can be separated into elastic and plastic components (Lloret-

184 Cabot et al. 2013), so the increment of total generalized strains can be expressed as:

$$185 \quad d\tilde{\boldsymbol{\varepsilon}} = d\tilde{\boldsymbol{\varepsilon}}^e + d\tilde{\boldsymbol{\varepsilon}}_j^p \quad \text{with } j = \text{LC}, \beta, \text{LC} + \beta; \beta = \text{SI} \text{ or } \text{SD} \quad (19)$$

186 where  $j$  is as defined in equation (16).

187 When only one elastic mechanism is activated, the generalized stress-strain  
188 relationship can be expressed as:

$$189 \quad d\boldsymbol{\sigma}^* = \mathbf{D}_e^* d\tilde{\boldsymbol{\varepsilon}}^e \quad (20)$$

190 where  $\mathbf{D}_e^*$  is the generalized elastic matrix written in terms of the elastic bulk modulus  
191  $K$ , the slope of the scanning curve in the water retention plane  $\kappa_s$  and the Poisson's  
192 ratio  $\mu$ . Full details of  $\mathbf{D}_e^*$  and  $\mathbf{D}_{ep}^*$ , the generalized elasto-plastic matrix, are presented  
193 in Appendix A.

194 There are nine parameters required in this microstructurally related constitutive  
195 model, namely  $\lambda$ ,  $\kappa$ ,  $k_1$ ,  $k_2$ ,  $M$ ,  $\mu$ ,  $\lambda_s$ ,  $\kappa_s$  and  $S_{\text{res}}$ .  $\lambda$  and  $\kappa$  are the slopes of  
196 normal consolidation line for saturated soil and slope of rebound curve, and they are  
197 related to the volumetric deformation during loading.  $k_1$  and  $k_2$  reflect the coupled  
198 movement between yield surfaces. To determine  $k_1$  and  $k_2$ , two sets of data where both  
199 plastic volumetric strain and plastic change of degree of saturation are witnessed during  
200 loading (the parameters can be determined by using this data to solve equation (17) and  
201 equation (18)).  $M$  is a parameter that represents the relationship between deviator  
202 stress and effective stress under critical state and can be acquired by considering  
203 standard triaxial test data.  $\mu$  is Poisson's ratio.  $\lambda_s$ ,  $\kappa_s$  and  $S_{\text{res}}$  are the slopes of the  
204 main drying/wetting curve, the slope of scanning curve and residual degree of saturation,

205 respectively. The residual degree of saturation can be gained by drawing two tangents  
206 at the start point and end point of the residual phase in a soil-water characteristic curve  
207 and taking the degree of saturation at the intersection as the residual degree of saturation  
208 (Eyo et al. 2022).

## 209 **MODEL VALIDATION**

210 To test the applicability of the proposed model, reported behaviour of a series of  
211 statically compacted samples of soils with double porosity (Speswhite kaolin, low-  
212 plastic clay and Jossigny silt) are considered. Speswhite kaolin is a low-expansive clay  
213 with dominant mineral as kaolinite and 75% clay fraction, which has a higher rate of  
214 consolidation compared with other clay soils (Sivakumar 1993). The low-plastic soil  
215 is a mixture of 40% Leighton Buzzard sand, 40% M400 silt and 20% Speswhite kaolin  
216 (Almahbobi, 2018). The soil showed significant collapsibility, in that it had a 16.2%  
217 vertical strain in a single oedometer test where the specimens were compacted at water  
218 content of 10% and dry unit weight of  $14\text{kN/m}^3$ , and applied vertical pressure was  
219 increased to 50kPa. The plasticity index is 8%. According to the Unified Soil  
220 Classification System (USCS), the soil can be classified as low-plastic clay. Jossigny  
221 silt originates from the eastern region of Paris and typically shows little swelling on  
222 wetting. The soil is composed of illite, kaolinite and interstratified illite-smectite. The  
223 liquid limit and plastic limit are 37% and 19%, respectively (Cui and Delage 1996).

224 Experimental data in terms of wetting, isotropic compression and shear response of  
225 these soils are used to validate the model's performance.

226 **Speswhite Kaolin**

227 *Isotropic compression*

228 Suction-controlled triaxial tests reported by Sivakumar (1993) on compacted  
229 samples of Speswhite kaolin and conducted under both isotropic compression and shear  
230 have been considered. For isotropic loading, Path 1 was carried out by compressing the  
231 initial sample (mean net stress  $\bar{p}=50\text{kPa}$ ) to  $\bar{p}=250\text{kPa}$  at a constant suction of 300kPa;  
232 Path 2 was carried out by wetting the initial sample (mean net stress  $\bar{p}=50\text{kPa}$ ) to  
233  $s=100\text{kPa}$  and then compressing it to  $\bar{p}=200\text{kPa}$  at a constant suction of 100kPa (see  
234 **Fig. 2**). Model parameters and initial states given by Lloret-Cabot et al. (2013) are  
235 shown in **Table 1**.

236 For both isotropic loading paths, the increasing net mean stress  $\bar{p}$  resulted in  
237 overall compression and a decrease in void ratio. As noted by Lloret-Cabot et al. (2013),  
238 the initial stress state lay on the SD yield surface for both paths. This meant that as the  
239 modified suction reduced, yielding invariably occurred on the SD yield surface, which  
240 brought about a coupled inward movement of the LC yield surface and downward  
241 movement of SI yield surface. Before yielding on the SD surface there was no  
242 significant change in the void ratio or degree of saturation mainly because the modified  
243 suction did not decrease rapidly. In path 1, when the mean effective stress reached about  
244 275kPa, the sample yielded on both the LC and SD yield surface. This yielding induced  
245 considerable amounts of plastic volumetric strain resulting in a significant decrease in  
246 void ratio (see **Fig. 3 (b)**). Since the yielding on the LC yield surface results in a coupled

247 upward movement of the SD yield surface, this also generated a significant increase in  
248 degree of saturation (see **Fig. 3** (c)). **Fig. 3** also presents a similar pattern of behaviour  
249 for Path 2. Overall, it can also be seen that the proposed model is able to reproduce  
250 well the isotropic loading behaviour of the Speswhite kaolin sample.

### 251 *Shear loading*

252 The loading of Speswhite kaolin samples included shear tests at constant confining  
253 stress and constant mean net stress. Both tests were carried out while suction remained  
254 unchanged. Before conducting the shear test at constant confining stress the sample was  
255 compressed from initial conditions of  $\bar{p}=50\text{kPa}$  and  $s=300\text{kPa}$  to  $\bar{p}=150\text{kPa}$ . The  
256 axial stress  $\sigma_1$  was then increased until reaching failure ( $\sigma_2=\sigma_3=150\text{kPa}$ ,  
257  $s=300\text{kPa}$ ). For shear tests at constant net mean stress, the loading path included  
258 wetting the initial sample ( $\bar{p}=50\text{kPa}$  and  $s=300\text{kPa}$ ) to  $s=100\text{kPa}$  and then compressing  
259 it to  $\bar{p}=200\text{kPa}$  before shearing it until failure. The model parameters and initial states  
260 are again as presented in **Table 1**.

261 **Fig. 4** shows the simulated and experimental results of shear tests at constant  
262 confining stress and net mean stress. The constant confining stress path yielded on both  
263 the LC and SD yield surface due to the previous isotropic compression where the net  
264 mean stress was increased to 150kPa. Yielding on the LC yield surface brought about  
265 significant plastic volumetric deformation and a decrease of void ratio (see **Fig. 4** (b)).  
266 Meanwhile, the coupled upward movement of the SD yield surface resulted in a  
267 significant increase in degree of saturation (see **Fig. 4** (c)). As shown in **Fig. 4**, the

268 simulated stress path is consistent with the experimental path, however the developed  
269 axial strain  $\varepsilon_a$  is larger compared with the observed behaviour. This over prediction of  
270 axial strain whilst a soil tends towards critical state is a previously reported  
271 phenomenon which is attributed to the deficiency of the Modified Camclay Model  
272 (Lloret-Cabot et al. 2013). Generally, it can be observed that the proposed model can  
273 satisfactorily reproduce the development of void ratio and degree of saturation during  
274 shear.

275 For the shear test at constant net mean stress, the yielding also occurred on the LC  
276 and SD yield surfaces and generated a large amount of plastic change of void ratio and  
277 degree of saturation (see **Fig. 4** (e) and (f)). Although the proposed model overestimates  
278 the axial strain at critical state (see **Fig. 4** (d)), it can generally represent the mechanical  
279 and hydraulic behaviour of the Speswhite kaolin sample.

## 280 **Low-Plastic Clay**

281 The soil samples were prepared by adding quantities of distilled water to dry  
282 mixtures with a target initial water content of 10%. Then the soil-water mixtures were  
283 compacted in a mould until an axial pressure equivalent to 998kPa was reached. The  
284 final dry unit weight of the soil samples was  $15\text{kN/m}^3$ . The measured initial void ratio,  
285 degree of saturation and suction were 0.732, 36.2% and 563kPa, respectively, and for  
286 the tests considered here the sample was first isotropically loaded under a confining  
287 stress of 20kPa. Model parameters and initial states are estimated from calibrating  
288 experimental data of wetting, isotropic compression and shear tests provided by

289 Almahbobi (2018).  $\lambda$ ,  $\kappa$ ,  $k_1$  and  $k_2$  are from isotropic compression tests.  $M$  is  
290 attained from shear tests and  $\mu$  is assumed to be 0.3.  $\lambda_s$ ,  $\kappa_s$  and  $S_{res}$  are obtained from  
291 the reported soil-water characteristic curve. Model parameters and initial states are  
292 shown in **Table 2**.

### 293 *Wetting*

294 The sample was initially wetted to a suction equivalent to 500kPa (at constant  
295 confining stress of 20kPa) and compressed to net mean stress equivalent to 100kPa (at  
296 constant suction of 500kPa), the suction of the sample was then decreased in a stepwise  
297 manner to 5kPa. Experimentally observed behaviour showed the void ratio  
298 monotonically decreasing during wetting, along with a decrease in effective stress. This  
299 behaviour is consistent with the highly collapsible nature of the soil (Almahbobi 2018).  
300 Degree of saturation increased significantly with suction decrease and was close to  
301 saturation at the final suction of 5kPa. The proposed model simulated yielding on both  
302 the LC and SD yield surfaces throughout the wetting stress path (the initial stress state  
303 was located at the corner intersection of both) leading to a prediction of a significant  
304 decrease in void ratio and increase of degree of saturation. The modelled behaviour is  
305 consistent with the experimental behaviour, with the model successfully reproducing  
306 the collapsibility and saturation increase observed during wetting (see **Fig. 5**).

### 307 *Isotropic compression*

308 For saturated compression, the initial samples were wetted to saturation at a  
309 confining stress of 20kPa and then compressed to target net mean stresses of 100, 250



310 and 400kPa, respectively.

311 **Table 3** compares experimentally reported and proposed model calculated void  
312 ratio and water content at the end of compression. Both the void ratio and water content  
313 decreased during compression due to the volumetric compression and water discharge  
314 induced by the increasing net mean stress. The differences between model results and  
315 experimental results are small with relative differences always less than 10% and below  
316 5% for some data. It can be seen that the model performs well when predicting the void  
317 ratio and water content in a saturated compression test (see **Table 3**).

318 For unsaturated compression, the initial samples were wetted to a suction equivalent  
319 to 300kPa at the confining stress of 20kPa and then compressed to target net mean  
320 stresses of 100, 250 and 400kPa. Experimental and model results are again shown in  
321 Table 3 and it can be seen that the model matches the experimental behaviour well  
322 (relative differences are around 1% for void ratio and less than 10% for degree of  
323 saturation), demonstrating the effectiveness of the model in reproducing hydro-  
324 mechanical behaviour in unsaturated compression (see **Table 3**).

### 325 *Shear loading*

326 After the compression stage described above each of the saturated and unsaturated  
327 samples were sheared at a constant confining stress equivalent to the net mean stress at  
328 the end of compression. The experimentally measured void ratio and water content at  
329 the start of the shear loading stage were used in the proposed model.

330 In the saturated shear tests the deviatoric stress was observed to increase with

331 increase in axial strain and reached a peak at an axial strain of 25%. The samples with  
332 higher confining stress had a higher peak of deviatoric stress. The peaks of deviatoric  
333 stress were 172, 436 and 660kPa, respectively, for the samples with confining stress  
334 equivalent to 100, 250 and 400kPa. The volumetric strain also increased and the sample  
335 with larger confining stress generated more significant volumetric deformation. In the  
336 model, the stress path remained yielding on both LC and SD yield surfaces and so  
337 volumetric strain developed further during shear. The modelled deviatoric stresses were  
338 consistent with the experimental results (see **Fig. 6(a)**). The model also performs well  
339 in terms of void ratios (see **Fig. 6 (b)**). Similar conclusions can also be drawn from the  
340 unsaturated shear tests with the model demonstrating satisfactory performance (see **Fig.**  
341 **6 (c), (d)**). For **Fig. 6 (d)**, the model satisfactorily reproduced the change of void ratio  
342 when the confining stress is 400kPa. However, whilst the model correctly captures the  
343 overall trends of decreasing volume during shear, it overpredicts the magnitude of  
344 changes in void ratio when the confining stresses are 100kPa and 250kPa.

#### 345 **Jossigny Silt**

346 Cui and Delage (Cui and Delage 1996) studied the yielding and plastic behaviour  
347 of unsaturated compacted samples of the Jossigny silt through isotropic compression  
348 and shear tests. According to the experimental results reported by Cui and Delage  
349 (1996),  $\lambda$ ,  $\kappa$ ,  $k_1$  and  $k_2$  are based on the isotropic compression tests.  $M$  is attained  
350 from shear tests and  $\mu$  is assumed to be 0.3.  $\lambda_s$  and  $\kappa_s$  are obtained from the reported  
351 soil-water characteristic curve. The model parameters and initial states are presented in

352 **Table 4.** The microscopic degree of saturation  $S_{res}$  was estimated by Alonso et al  
353 (2010).

354 The samples were firstly wetted to target suctions (200, 400, 800 and 1500kPa) and  
355 then compressed to target net mean stresses (50, 100, 200, 400 and 600kPa) before they  
356 were sheared at constant cell pressures (50, 100, 200, 400 and 600kPa). The shear stage  
357 terminated when the critical state was reached.

#### 358 *Isotropic compression*

359 **Table 5** presents the comparison between model results and experimental results  
360 for isotropic compression at both a constant suction equivalent to 200kPa and at a  
361 constant net mean stress equivalent to 200kPa. It can be concluded that the model  
362 performs well in isotropic compression with the simulated development of void ratio  
363 and degree of saturation satisfactorily consistent with the experimental results.

#### 364 *Shear*

365 Shear tests were conducted after the target suctions and net mean stresses were  
366 reached in the compression tests mentioned above. Shear tests continued until the  
367 critical state was reached. **Fig. 7** presents the deviatoric stress/void ratio-axial strain  
368 relationship in shear tests at constant suction equivalent to 200kPa and **Table 6** shows  
369 the comparison on degree of saturation between model results and experimental results  
370 when critical states are reached.

371 In general, the model can reproduce the changing trend of deviatoric stress with  
372 respect to the axial strain despite the model tending to overestimate the axial strain at a

373 specific deviatoric stress (see **Fig. 7** (a)). The model also performs well in predicting  
374 the trends in degree of saturation (see **Table 6**) during shear but does overpredict the  
375 magnitude of the change of void ratio, as shown in **Fig. 7** (b). It is noted that as the  
376 wetting and compression steps, undertaken before shearing commenced, are also  
377 included in the simulation there is different in the predicted and measured void ratios  
378 at zero axial strain. It can also be noticed in **Fig. 7** (a) that there are discontinuities of  
379 the gradient for shear tests at cell pressure equivalent to 50 and 200kPa because the  
380 stress paths for these tests reached the LC yield surface during shearing. The stress path  
381 for the shear test at cell pressure equivalent to 600kPa had reached the LC yield surface  
382 during the isotropic compression stage so there is no discontinuity observed on the  
383 curve.

384 For shear tests at constant cell pressure equivalent to 200kPa, **Fig. 7** (c), (d) present  
385 the deviatoric stress/void ratio-axial strain relationship and **Table 6** shows the  
386 comparison on degree of saturation between model results and experimental results at  
387 the end of shear tests. It is clear that the model performs well under different suctions  
388 by satisfactorily reproducing the trends of behaviour but does exhibit a tendency to  
389 overpredict the magnitude of changes in void ratio.

## 390 **CONCLUSIONS**

391 A hydro-mechanical coupled constitutive model for unsaturated soils with double  
392 porosity is proposed in this paper, based on the framework of Glasgow Coupled Model.  
393 Since the Glasgow Coupled Model does not consider microstructure, the model

394 established in this paper adopts effective degree of saturation as a microstructural index  
395 and introduces this index into Bishop's effective stress to establish the Bishop's  
396 effective stress formula that can consider the characteristics of the double porosity. The  
397 model also adopted the Modified Camclay Model in the average effective stress-  
398 deviatoric stress plane. The expressions of the model were derived by combining the  
399 generalized stress-strain tensor, associated flow law, hardening law and consistency  
400 conditions. The novelty of the established model lies in the combination of effective  
401 degree of saturation, Glasgow Coupled Model and Modified Camclay Model to provide  
402 a convenient and straightforward way to model the behaviour of double-porosity soils  
403 utilising only nine physically meaningful parameters.

404 The model has been validated against experimentally observed behaviour of  
405 double-porosity samples, such as the compacted samples of Speswhite kaolin (low-  
406 expansive), low-plastic clay (highly collapsible) and Jossigny silt (non-expansive). The  
407 validation results show that the model is able to predict with reasonable accuracy the  
408 hydro-mechanical coupled characteristics of unsaturated soils with double porosity,  
409 whether the soil is collapsible or non-expansive. In terms of isotropic compression and  
410 wetting behaviour, the model satisfactorily reproduces both the mechanical behaviour  
411 (the variation of the modified suction and the void ratio) and hydraulic behaviour (the  
412 variation of degree of saturation). The model also performs well in terms of shear  
413 response. The model results are generally consistent with the experimental results in  
414 terms of void ratio and degree of saturation, but the model, to some extent, overpredicts

415 the axial strain at specific deviatoric stress. This feature is not unexpected as the  
416 Modified Camclay Model usually overestimates the axial strain developed during shear  
417 on the path to reach critical state. Overall, it is demonstrated that the inclusion of  
418 effective degree of saturation in such model is beneficial to consider the effect of  
419 microstructure, especially double porosity, on the behaviour of unsaturated soils and  
420 the proposed model is reliable in predicting the hydro-mechanical coupled behaviour  
421 of collapsible and non-expansive soils with double porosity.

422

## 423 APPENDIX A

424 The full expression for  $\mathbf{D}_e^*$  is given as follows:

$$425 \quad \mathbf{D}_e^* = \begin{pmatrix} E_{11} & E_{12} & E_{13} & 0 & 0 & 0 & 0 \\ E_{21} & E_{22} & E_{23} & 0 & 0 & 0 & 0 \\ E_{31} & E_{32} & E_{33} & 0 & 0 & 0 & 0 \\ 0 & 0 & 0 & E_{44} & 0 & 0 & 0 \\ 0 & 0 & 0 & 0 & E_{55} & 0 & 0 \\ 0 & 0 & 0 & 0 & 0 & E_{66} & 0 \\ 0 & 0 & 0 & 0 & 0 & 0 & E_{77} \end{pmatrix} = \begin{pmatrix} \mathbf{D}_e^{6 \times 6} & \mathbf{0} \\ \mathbf{0} & \gamma_e^{1 \times 1} \end{pmatrix} \quad (21)$$

$$426 \quad E_{11} = E_{22} = E_{33} = K + \frac{4}{3G} = \left( \frac{\nu}{\kappa} \right) p^* + \frac{4}{3G} \quad (22)$$

$$427 \quad E_{44} = E_{55} = E_{66} = G = \frac{3K(1-2\mu)}{2(1+\mu)} \quad (23)$$

$$428 \quad E_{12} = E_{23} = E_{13} = K - \frac{2}{3G} \quad (24)$$

$$429 \quad E_{77} = \gamma_e = \left( \frac{1}{\kappa_s} \right) s^* \quad (25)$$

430 where  $K$  is the bulk modulus and  $G$  is the shear modulus.

431 When a plastic mechanism is active, the generalized stress-strain relationship can

432 be also assumed as follows:

$$433 \quad d\boldsymbol{\sigma}^* = \mathbf{D}_e^* d\tilde{\boldsymbol{\varepsilon}}^e = \mathbf{D}_{ep}^* d\tilde{\boldsymbol{\varepsilon}} \quad (26)$$

434  $\mathbf{D}_{ep}^*$  is the generalized elasto-plastic matrix, depending on the specific plastic  
 435 mechanism(s) active during loading.  $\mathbf{D}_{ep}^*$  is unknown hitherto, but the expression of it  
 436 can be obtained by the following approach.

437 Considering the general case that two plastic mechanisms are active, the expression  
 438 (26) can be written as

$$439 \quad d\boldsymbol{\sigma}^* = \mathbf{D}_e^* d\tilde{\boldsymbol{\varepsilon}}^e = \mathbf{D}_e^* \left( d\tilde{\boldsymbol{\varepsilon}} - d\tilde{\boldsymbol{\varepsilon}}_{LC+\beta}^p \right) \quad (27)$$

440 Then considering the flow rule (16),

$$441 \quad d\tilde{\boldsymbol{\varepsilon}}_{LC+\beta}^p = d\lambda_{LC}^{LC+\beta} \frac{\partial F_{LC}}{\partial \boldsymbol{\sigma}^*} + d\lambda_{\beta}^{LC+\beta} \frac{\partial F_{\beta}}{\partial \boldsymbol{\sigma}^*} \quad (28)$$

442 To keep the end of the stress path invariably attached on yield surfaces after yielding,  
 443 the consistency condition on  $F_{LC}$  and  $F_{\beta}$  should be considered:

$$444 \quad dF_{LC} = \left( \frac{\partial F_{LC}}{\partial \boldsymbol{\sigma}^*} \right)^T d\boldsymbol{\sigma}^* + \frac{\partial F_{LC}}{\partial p_0^*} dp_0^* = 0 \quad (29)$$

$$445 \quad dF_{\beta} = \left( \frac{\partial F_{\beta}}{\partial s^*} \right)^T ds^* + \frac{\partial F_{\beta}}{\partial s_{\beta}^*} ds_{\beta}^* = 0 \quad (30)$$

446 Incorporating (29), (30) and hardening laws (17) and (18), the following  
 447 expressions can be obtained:

$$448 \quad \left( \frac{\partial F_{\beta}}{\partial s^*} \right)^T (-\gamma_e) \left( ds_e - d\lambda_{\beta}^{LC+\beta} \frac{\partial F_{\beta}}{\partial s^*} \right) + \frac{\partial F_{\beta}}{\partial s_{\beta}^*} s_{\beta}^* \left[ -\frac{d\lambda_{\beta}^{LC+\beta} \frac{\partial F_{\beta}}{\partial s^*}}{\lambda_s - \kappa_s} + k_2 \frac{vm^T d\lambda_{LC}^{LC+\beta} \frac{\partial F_{LC}}{\partial \boldsymbol{\sigma}^*}}{\lambda - \kappa} \right] = 0 \quad (31)$$

450  
 451

$$452 \quad \left( \frac{\partial F_{LC}}{\partial \boldsymbol{\sigma}^*} \right)^T \mathbf{D}_e \left( d\boldsymbol{\varepsilon} - d\chi_{LC}^{LC+\beta} \frac{\partial F_{LC}}{\partial \boldsymbol{\sigma}^*} \right) + \frac{\partial F_{LC}}{\partial p_o^*} p_o^* \left[ v \frac{m^T d\lambda_{LC}^{LC+\beta} \frac{\partial F_{LC}}{\partial \boldsymbol{\sigma}^*}}{\lambda - \kappa} - \frac{k_1 d\lambda_{\beta}^{LC+\beta} \frac{\partial F_{\beta}}{\partial s^*}}{\lambda_s - \kappa_s} \right] = 0 \quad (32)$$

453 Then the plastic multipliers can be derived as:

$$454 \quad d\lambda_{LC}^{LC+\beta} = \frac{\mathbf{a}_{LC+\beta}^T d\boldsymbol{\varepsilon} + b_{LC+\beta} dS_e}{h_{LC+\beta}} \quad (33)$$

$$455 \quad d\lambda_{\beta}^{LC+\beta} = \frac{\mathbf{c}_{LC+\beta}^T d\boldsymbol{\varepsilon} + d_{LC+\beta} dS_e}{h_{LC+\beta}} \quad (34)$$

456 where

$$457 \quad \mathbf{a}_{LC+\beta}^T = \left( \frac{\partial F_{LC}}{\partial \boldsymbol{\sigma}^*} \right)^T \mathbf{D}_e \left( \frac{\partial F_{\beta}}{\partial s^*} \gamma_e \frac{\partial F_{\beta}}{\partial s^*} - \frac{\partial F_{\beta}}{\partial s_{\beta}^*} s_{\beta}^* \frac{1}{\lambda_s - \kappa_s} \frac{\partial F_{\beta}}{\partial s^*} \right) \quad (35)$$

$$458 \quad b_{LC+\beta} = -k_1 \frac{\partial F_{\beta}}{\partial s^*} \gamma_e \frac{\partial F_{LC}}{\partial p_o^*} \frac{p_o^*}{\lambda_s - \kappa_s} \frac{\partial F_{\beta}}{\partial s^*} \quad (36)$$

$$459 \quad \mathbf{c}_{LC+\beta}^T = k_2 \left( \frac{\partial F_{LC}}{\partial \boldsymbol{\sigma}^*} \right)^T \mathbf{D}_e \frac{\partial F_{\beta}}{\partial s_{\beta}^*} v \frac{s_{\beta}^*}{\lambda - \kappa} m^T \frac{\partial F_{LC}}{\partial \boldsymbol{\sigma}^*} \quad (37)$$

$$460 \quad d_{LC+\beta} = \frac{\partial F_{\beta}}{\partial s^*} \gamma_e \left( - \left( \frac{\partial F_{LC}}{\partial \boldsymbol{\sigma}^*} \right)^T \mathbf{D}_e \frac{\partial F_{LC}}{\partial \boldsymbol{\sigma}^*} + \frac{\partial F_{LC}}{\partial p_o^*} \frac{v}{\lambda - \kappa} m^T \frac{\partial F_{LC}}{\partial \boldsymbol{\sigma}^*} \right) \quad (38)$$

$$461 \quad h_{LC+\beta} = \left[ - \left( \frac{\partial F_{LC}}{\partial \boldsymbol{\sigma}^*} \right)^T \mathbf{D}_e \frac{\partial F_{LC}}{\partial \boldsymbol{\sigma}^*} + \frac{\partial F_{LC}}{\partial p_o^*} \frac{v}{\lambda - \kappa} p_o^* m^T \frac{\partial F_{LC}}{\partial \boldsymbol{\sigma}^*} \right] \\ * \left[ - \frac{\partial F_{\beta}}{\partial s^*} \gamma_e \frac{\partial F_{\beta}}{\partial s^*} + \frac{\partial F_{\beta}}{\partial s_{\beta}^*} s_{\beta}^* \frac{1}{\lambda_s - \kappa_s} \frac{\partial F_{\beta}}{\partial s^*} \right] \\ - k_1 k_2 \frac{\partial F_{\beta}}{\partial s_{\beta}^*} p_o^* \frac{v}{\lambda - \kappa} s_{\beta}^* \frac{1}{\lambda_s - \kappa_s} \frac{\partial F_{LC}}{\partial p_o^*} m^T \frac{\partial F_{LC}}{\partial \boldsymbol{\sigma}^*} \frac{\partial F_{\beta}}{\partial s^*} \quad (39)$$

462 Substituting these two plastic multipliers (33) and (34) into (26) and after some

463 algebra, the generalized elasto-plastic matrix can be obtained as follows:

$$464 \quad \mathbf{D}_{ep}^* = \begin{pmatrix} \mathbf{A}_{LC+\beta} & \mathbf{B}_{LC+\beta} \\ \left( \mathbf{C}_{LC+\beta} \right)^T & D_{LC+\beta} \end{pmatrix} \quad (40)$$

465 where



466 
$$\mathbf{A}_{\text{LC}+\beta} = \mathbf{D}_e \left( \mathbf{I}_{6 \times 6} - \frac{\mathbf{a}_{\text{LC}+\beta}^T}{h_{\text{LC}+\beta}} \frac{\partial F_{\text{LC}}}{\partial \boldsymbol{\sigma}^*} \right) \quad (41)$$

467 
$$\mathbf{B}_{\text{LC}+\beta} = \mathbf{D}_e \left( \frac{\partial F_{\text{LC}}}{\partial \boldsymbol{\sigma}^*} \frac{b_{\text{LC}+\beta}}{h_{\text{LC}+\beta}} \right) \quad (42)$$

468 
$$\left( \mathbf{C}_{\text{LC}+\beta} \right)^T = -\gamma_e \left( \frac{\partial F_{\beta}}{\partial s^*} \frac{\mathbf{c}_{\text{LC}+\beta}^T}{h_{\text{LC}+\beta}} \right) \quad (43)$$

469 
$$D_{\text{LC}+\beta} = \gamma_e \left( 1 + \frac{\partial F_{\beta}}{\partial s^*} \frac{d_{\text{LC}+\beta}}{h_{\text{LC}+\beta}} \right) \quad (44)$$

470 **DATA AVAILABILITY STATEMENT**

471 All data, models, or code that support the findings of this study are available from  
 472 the corresponding author upon reasonable request.

473 **ACKNOWLEDGEMENTS**

474 This research was financially supported by the National Natural Science Foundation  
 475 of China (U2034204, 52078031, U1834206), the Natural Science Foundation of  
 476 Beijing Municipality (8202038), Fundamental Research Funds for the Central  
 477 Universities (2021CZ109, 2021JBZ111), and the China Scholarship Council (CSC)  
 478 from the Ministry of Education of P.R. China (CSC202007090010)

479

480 **REFERENCES**

481 Alazaiza, M. Y. D., Ngien, S. K., Bob, M. M., Kamaruddin, S. A., and Ishak, W. M.  
 482 F.2017. "Influence of Macro-pores on DNAPL Migration in Double-Porosity  
 483 Soil Using Light Transmission Visualization Method." *Transp. Porous Media*,  
 484 117(1), 103–123. <https://doi.org/10.1007/s11242-017-0822-3>.

485 Almahbobi, S. A.2018. “Experimental study of volume change and shear strength  
486 behaviour of statically compacted collapsible soil.” Cardiff University, UK.

487 Alonso, E. E., Pereira, J.-M., Vaunat, J., and Olivella, S.2010. “A microstructurally  
488 based effective stress for unsaturated soils.” *Géotechnique*, 60(12), 913–925.  
489 <https://doi.org/10.1680/geot.8.P.002>.

490 Bagherieh, A. R., Khalili, N., Habibagahi, G., and Ghahramani, A.2009. “Drying  
491 response and effective stress in a double porosity aggregated soil.” *Eng. Geol.*,  
492 105(1), 44–50. <https://doi.org/10.1016/j.enggeo.2008.12.009>.

493 Bishop, A. W.1959. “The Principle of Effective Stress.” *Tek. Ukebl.*, 39, 859–863.

494 Cai, G., He, X., Dong, L., Liu, S., and Sheng, D.2020a. “The shear and tensile strength  
495 of unsaturated soils by a grain-scale investigation.” *Granul. Matter*, 22(1)  
496 <https://doi.org/10.1007/s10035-019-0969-4>.

497 Cai, G. Q., Wang, Y. N., Zhou, A. N., and Zhao, C. G.2018. “A microstructure-  
498 dependent hydro-mechanical coupled constitutive model for unsaturated soils.”  
499 *Chin. J. Geotech. Eng.*, 40(04), 618–624.  
500 <https://doi.org/10.11779/CJGE201804005>.

501 Cai, G., Zhou, A., Liu, Y., Xu, R., and Zhao, C.2020b. “Soil water retention behavior  
502 and microstructure evolution of lateritic soil in the suction range of 0–  
503 286.7MPa.” *Acta Geotech.*, 15, 3327–3341. [https://doi.org/10.1007/s11440-  
504 020-01011-w](https://doi.org/10.1007/s11440-020-01011-w).

505 Cai, G., Zhou, A., and Sheng, D.2014. “Permeability function for unsaturated soils with

506 different initial densities.” *Can. Geotech. J.*, 51(12), 1456–1467.  
507 <https://doi.org/10.1139/cgj-2013-0410>.

508 Casini, F., Vaunat, J., Romero, E., and Desideri, A.2012. “Consequences on water  
509 retention properties of double-porosity features in a compacted silt.” *Acta*  
510 *Geotech.*, 7(2), 139–150. <https://doi.org/10.1007/s11440-012-0159-6>.

511 Cui, Y. J., and Delage, P.1996. “Yielding and plastic behaviour of an unsaturated  
512 compacted silt.” *Géotechnique*, 46(2), 291–311.  
513 <https://doi.org/10.1680/geot.1996.46.2.291>.

514 Cuisinier, O., Auriol, J.-C., Le Borgne, T., and Deneele, D.2011. “Microstructure and  
515 hydraulic conductivity of a compacted lime-treated soil.” *Eng. Geol.*, 123(3),  
516 187–193. <https://doi.org/10.1016/j.enggeo.2011.07.010>.

517 Eyo, E. U., Ng’ambi, S., and Abbey, S. J.2022. “An overview of soil–water  
518 characteristic curves of stabilised soils and their influential factors.” *J. King*  
519 *Saud Univ. - Eng. Sci.*, 34(1), 31–45.  
520 <https://doi.org/10.1016/j.jksues.2020.07.013>.

521 Houlby, G. T.1997. “The work input to an unsaturated granular material.”  
522 *Geotechnique*, 47(1), 193–196. <https://doi.org/10.1680/geot.1997.47.1.193>.

523 Jia, R., Lei, H., and Li, K.2020. “Compressibility and Microstructure Evolution of  
524 Different Reconstituted Clays during 1D Compression.” *Int. J. Geomech.*,  
525 20(10), 04020181. [https://doi.org/10.1061/\(ASCE\)GM.1943-5622.0001830](https://doi.org/10.1061/(ASCE)GM.1943-5622.0001830).

526 Lewandowska, J., Szymkiewicz, A., Burzyński, K., and Vauclin, M.2004. “Modeling

527 of unsaturated water flow in double-porosity soils by the homogenization  
528 approach.” *Adv. Water Resour.*, 27(3), 283–296.  
529 <https://doi.org/10.1016/j.advwatres.2003.12.004>.

530 Li, J., Yin, Z.-Y., Cui, Y.-J., Liu, K., and Yin, J.-H.2019. “An elasto-plastic model of  
531 unsaturated soil with an explicit degree of saturation-dependent CSL.” *Eng.  
532 Geol.*, 260, 105240. <https://doi.org/10.1016/j.enggeo.2019.105240>.

533 Li, J., Zhao, C., Cai, G., Asreazad, S., Xu, X. F., and Huang, Q.2013. “The input work  
534 expression and the thermodynamics-based modelling framework for  
535 unsaturated expansive soils with double porosity.” *Chin. Sci. Bull.*, 58(27),  
536 3422–3429. <https://doi.org/10.1007/s11434-013-5828-9>.

537 Lloret-Cabot, M., Sánchez, M., and Wheeler, S. J.2013. “Formulation of a three-  
538 dimensional constitutive model for unsaturated soils incorporating mechanical-  
539 water retention couplings: A 3D COUPLED CONSTITUTIVE MODEL FOR  
540 UNSATURATED SOILS.” *Int. J. Numer. Anal. Methods Geomech.*, 37(17),  
541 3008–3035. <https://doi.org/10.1002/nag.2176>.

542 Low, H.-E., Phoon, K.-K., Tan, T.-S., and Leroueil, S.2008. “Effect of soil  
543 microstructure on the compressibility of natural Singapore marine clay.” *Can.  
544 Geotech. J.*, 45(2), 161–176. <https://doi.org/10.1139/T07-075>.

545 Manahiloh, K. N., Muhunthan, B., and Likos, W. J.2016. “Microstructure-based  
546 effective stress formulation for unsaturated granular soils.” *Int. J. Geomech.*,  
547 16(6), D4016006. [https://doi.org/10.1061/\(ASCE\)GM.1943-5622.0000617](https://doi.org/10.1061/(ASCE)GM.1943-5622.0000617).

548 Mašín, D.2013. “Double structure hydromechanical coupling formalism and a model  
549 for unsaturated expansive clays.” *Eng. Geol.*, 165, 73–88.  
550 <https://doi.org/10.1016/j.enggeo.2013.05.026>.

551 Mašín, D., Herbstová, V., and Boháč, J.2005. “Properties of double porosity clayfills  
552 and suitable constitutive models.” *Proc. 16th Int. Conf. Soil Mech. Geotech.*  
553 *Eng.*, IOS Press, 827–830. <https://doi.org/10.3233/978-1-61499-656-9-827>.

554 Musso, G., Romero, E., and Della Vecchia, G.2014. “Double-structure effects on the  
555 chemo-hydro-mechanical behaviour of a compacted active clay.” *Bio- Chemo-*  
556 *Mech. Process. Geotech. Eng.*, Conference Proceedings, ICE Publishing, 3–17  
557 <https://doi.org/10.1680/bcmpge.60531.001>.

558 Ngien, S. K., Rahman, N. A., Ahmad, K., Rol, and Lewis, W.2012. “A review of  
559 experimental studies on double-porosity soils.” *Sci. Res. Essays*, Academic  
560 Journals, 7(38), 3243–3250. <https://doi.org/10.5897/SRE11.2131>.

561 Ranaivomanana, H., Razakamanantsoa, A., and Amiri, O.2017. “Permeability  
562 prediction of soils including degree of compaction and microstructure.” *Int. J.*  
563 *Geomech.*, 17(4), 04016107. [https://doi.org/10.1061/\(ASCE\)GM.1943-](https://doi.org/10.1061/(ASCE)GM.1943-5622.0000792)  
564 [5622.0000792](https://doi.org/10.1061/(ASCE)GM.1943-5622.0000792).

565 Romero, E., and Simms, P. H.2008. “Microstructure investigation in unsaturated soils:  
566 a review with special attention to contribution of mercury intrusion porosimetry  
567 and environmental scanning electron microscopy.” *Geotech. Geol. Eng.*, 26(6),  
568 705–727. <https://doi.org/10.1007/s10706-008-9204-5>.

569 Roscoe, K., and Burland, J. B.1968. “On the generalized stress-strain behaviour of wet  
570 clay.” *Eng. Plast.*, 535–609.

571 Russell, A. R.2010. “Water retention characteristics of soils with double porosity.” *Eur.*  
572 *J. Soil Sci.*, 61(3), 412–424. <https://doi.org/10.1111/j.1365-2389.2010.01237.x>.

573 Sánchez, M., Gens, A., Villar, M. V., and Olivella, S.2016. “Fully coupled thermo-  
574 hydro-mechanical double-porosity formulation for unsaturated soils.” *Int. J.*  
575 *Geomech.*, 16(6), D4016015. [https://doi.org/10.1061/\(ASCE\)GM.1943-5622.0000728](https://doi.org/10.1061/(ASCE)GM.1943-5622.0000728).

577 Sergeev, Y. M., Grabowska-Olszewska, B., Osipov, V. I., Sokolov, V. N., and  
578 Kolomenski, Y. N.1980. “The classification of microstructures of clay soils.” *J.*  
579 *Microsc.*, 120(3), 237–260. <https://doi.org/10.1111/j.1365-2818.1980.tb04146.x>.

581 Sivakumar, V.1993. “A critical state framework for unsaturated soil.” University of  
582 Sheffield, United Kingdom.

583 Tian-er, M. A. O., and Lin, X. I. A.2010. “Experimental research on microstructure of  
584 expansive soil in north of Hubei province.” *J. Huazhong Univ. Sci. Technol.*  
585 *Urban Sci. Ed.*, 2 [https://en.cnki.com.cn/Article\\_en/CJFDTotal-WHCJ201002012.htm](https://en.cnki.com.cn/Article_en/CJFDTotal-WHCJ201002012.htm).

587 Trzciński, J., and Wójcik, E.2019. “Application of microstructure classification for the  
588 assessment of the variability of geological-engineering and pore space  
589 properties in clay soils.” *Open Geosci.*, 11(1), 236–248.

590 <https://doi.org/10.1515/geo-2019-0019>.

591 Wheeler, S. J., Sharma, R. S., and Buisson, M. S. R.2003. “Coupling of hydraulic

592 hysteresis and stress–strain behaviour in unsaturated soils.” 53(1), 41–54.

593 <https://doi.org/10.1680/geot.2003.53.1.41>.

594

595

596

597

598 **Table 1.** Model parameters and initial states for Speswhite kaolin (Lloret-Cabot et al.

599 2013)

Parameters		Initial states	
$\lambda$	0.124	$\bar{p}$ / kPa	50.00
$\kappa$	0.006	$s$ / kPa	300.00
$\lambda_s$	0.098	$e$	1.208
$\kappa_s$	0.0076	$S_r$	60.1%
$k_1$	0.662	$S_r^m$	5.0%
$k_2$	0.803	$p_0^*$ / kPa	273.00
$M$	0.71	$S_D^*$ / kPa	164.00
$\mu$	0.3	$S_1^*$ / kPa	/

600 **Table 2.** Model parameters and initial states for the mixture

Parameters		Initial states	
$\lambda$	0.07	$\bar{p}$ / kPa	20.00
$\kappa$	0.008	$s$ / kPa	563.00
$\lambda_s$	0.12	$e$	0.732
$\kappa_s$	0.02	$S_r$	36.2%
$k_1$	0.6	$S_r^m$	10.0%
$k_2$	0.3	$p_0^*$ / kPa	250.00
$M$	1.076	$S_D^*$ / kPa	237.94
$\mu$	0.3	$S_1^*$ / kPa	/

601 **Table 3.** Void ratios and water contents/degrees of saturation at the end of saturated  
602 and unsaturated compression

	$P_{\text{net}}$ (kPa)	$e$ (model)	$e$ (experiment)	$w$ (model)	$w$ (experiment)
Saturated	100	0.579	0.529	21.87%	19.90%
	250	0.490	0.476	18.49%	17.90%
	400	0.439	0.438	16.58%	16.50%
Unsaturated				$S_r$ (model)	$S_r$ (experiment)
	100	0.713	0.702	43.8%	40.7%
	250	0.665	0.661	46.2%	42.2%
	400	0.632	0.626	47.8%	43.6%

603 **Table 4.** Model parameters and initial states for the Jossigny silt samples

Parameters		Initial states	
$\lambda$	0.091	$\bar{p}$ / kPa	25.00
$\kappa$	0.013	$s$ / kPa	200.00
$\lambda_s$	0.131	$e$	0.629
$\kappa_s$	0.008	$S_r$	76.4%
$k_1$	0.65	$S_r^m$	56.0%
$k_2$	0.66	$p_0^*$ / kPa	374.60
$M$	1.02	$S_D^*$ / kPa	77.23
$\mu$	0.3	$S_I^*$ / kPa	103.84

604 **Table 5.** Results for the compression at constant suction/net mean stress

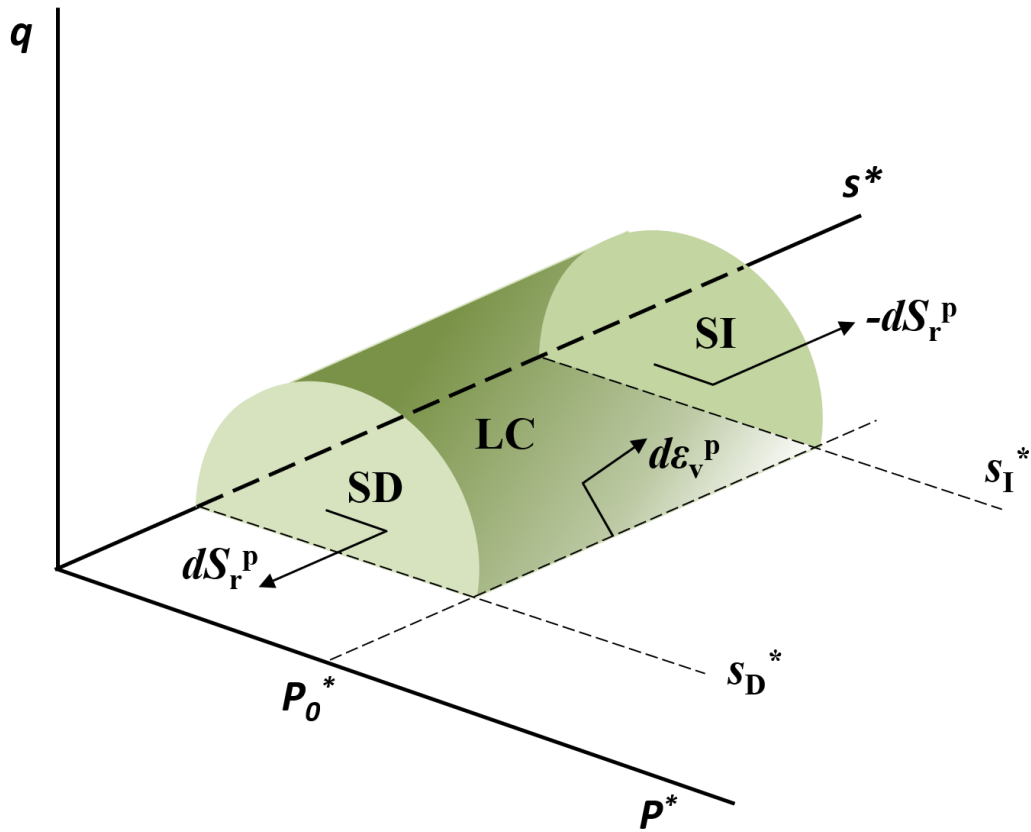
$s$ (kPa)	$p_{\text{net}}$ (kPa)	$e$ (model)	$e$ (experiment)	$S_r$ (model)	$S_r$ (experiment)
200	600	0.502	0.569	82.0%	84.0%
200	200	0.617	0.599	76.5%	77.0%
200	50	0.626	0.621	76.4%	77.0%
400	200	0.545	0.577	75.1%	74.0%
800	200	0.570	0.599	70.1%	70.0%

605 **Table 6.** Results of degree of saturation in the critical state

$s$ /kPa	$\sigma_3$ /kPa	$S_r$ (model)	$S_r$ (experiment)
200	600	94.3%	98.0%
200	200	85.7%	79.0%
200	50	79.2%	79.0%
400	200	76.3%	77.0%
800	200	70.1%	70.0%

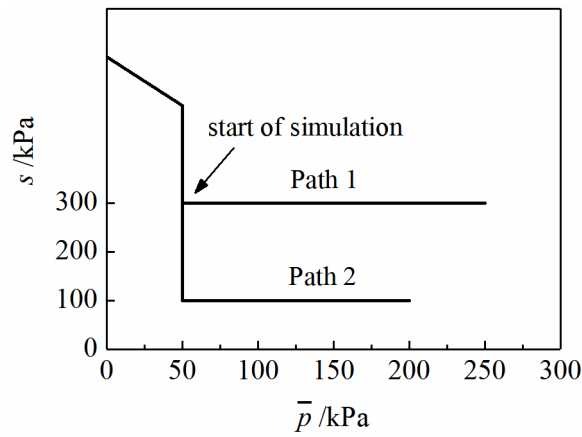
606





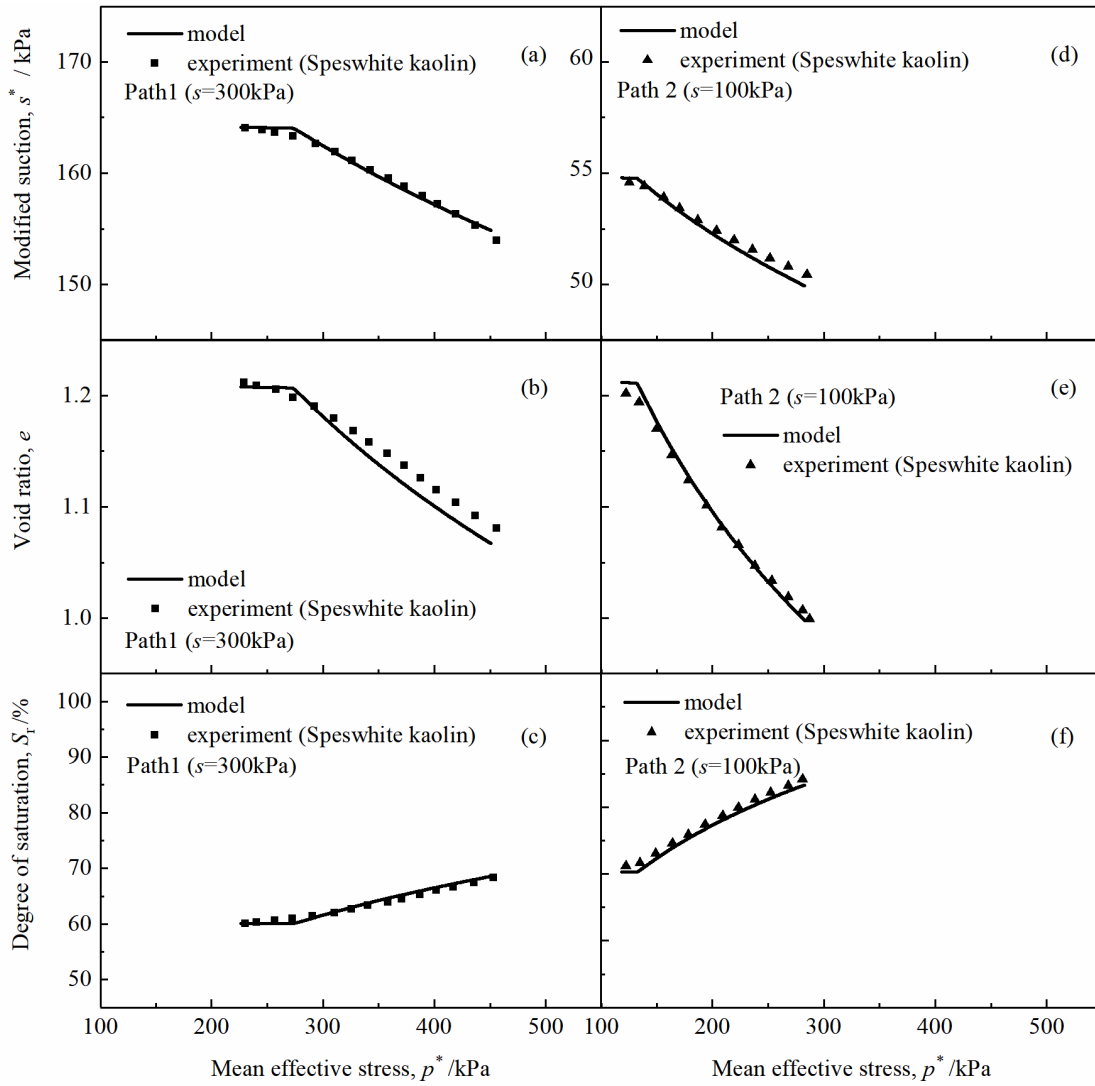
607

608 **Fig. 1.** Yield surfaces of the 3D generalized model (after Lloret-Cabot et al., 2013)



609

610 **Fig. 2.** Isotropic loading paths conducted by Sivakumar (Sivakumar, 1993)



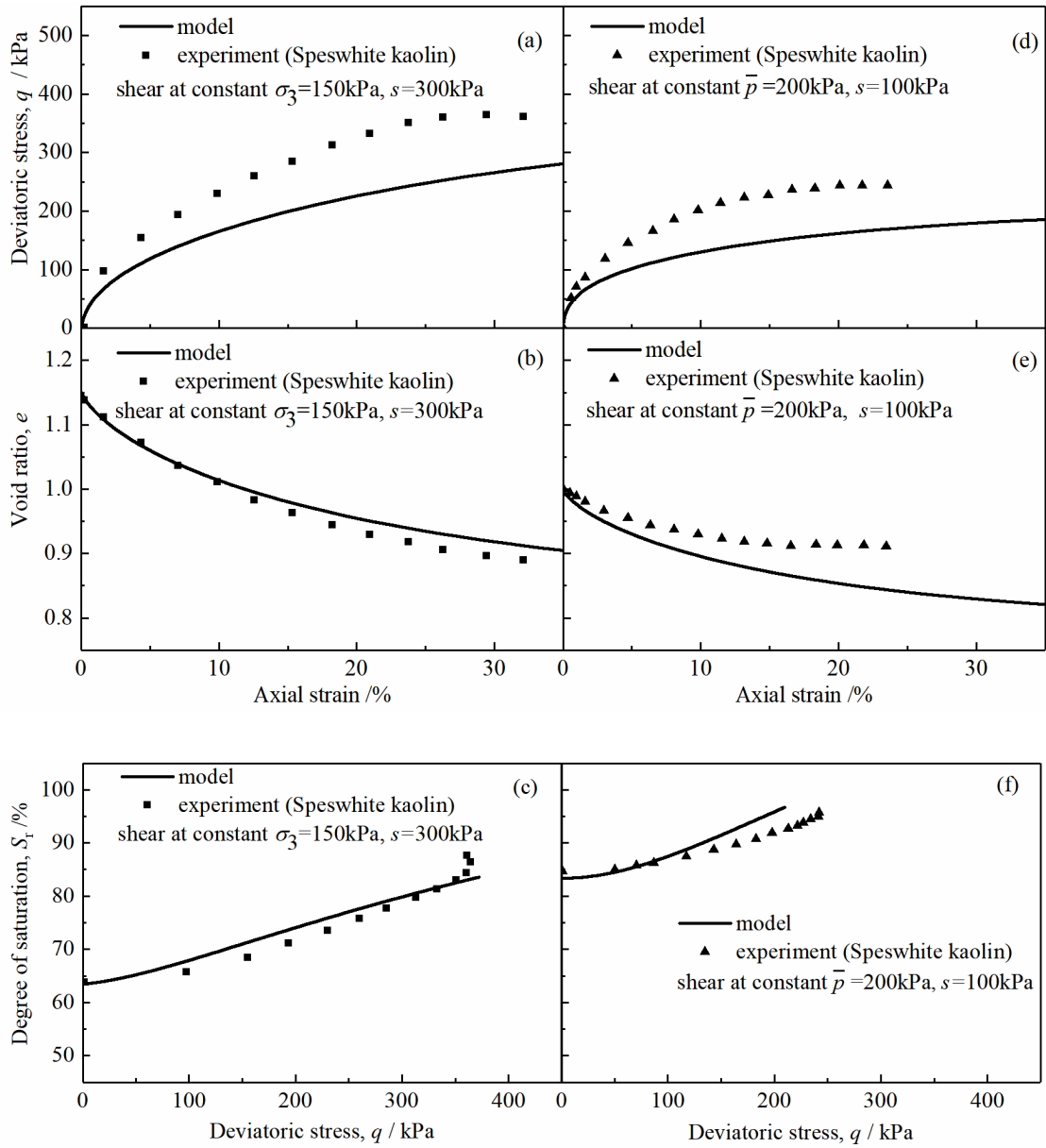
611

612 **Fig. 3.** Comparison between model results and experimental results on Speswhite

613 kaolin (Sivakumar, 1993) for Path 1 and Path 2: (a/d)  $p^* - s^*$ ; (b/e)  $p^* - e$ ; (c/f)

614

$$p^* - S_r$$



615

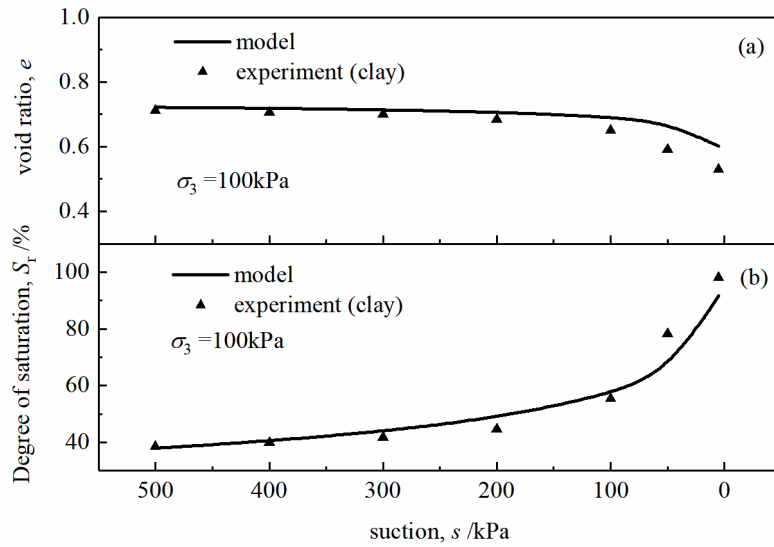
616

617 **Fig. 4.** Comparison between model results and experimental results (Sivakumar 1993)

618 for shear at constant confining stress and net mean stress: (a/d)  $\varepsilon_a - q$ ; (b/e)  $\varepsilon_a - e$ ;

619

(c/f)  $q - S_r$

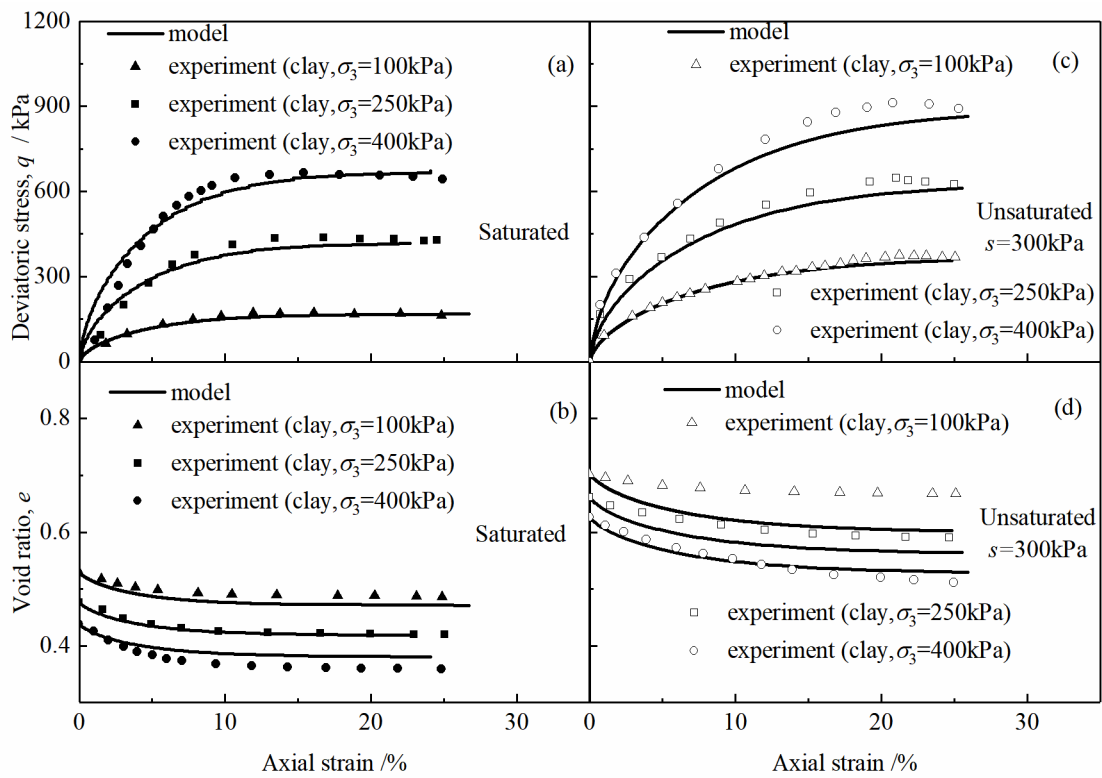


620

621 **Fig. 5.** Comparison between model results and experimental results on low-plastic

622

clay: (a)  $s - e$  ; (b)  $s - S_r$

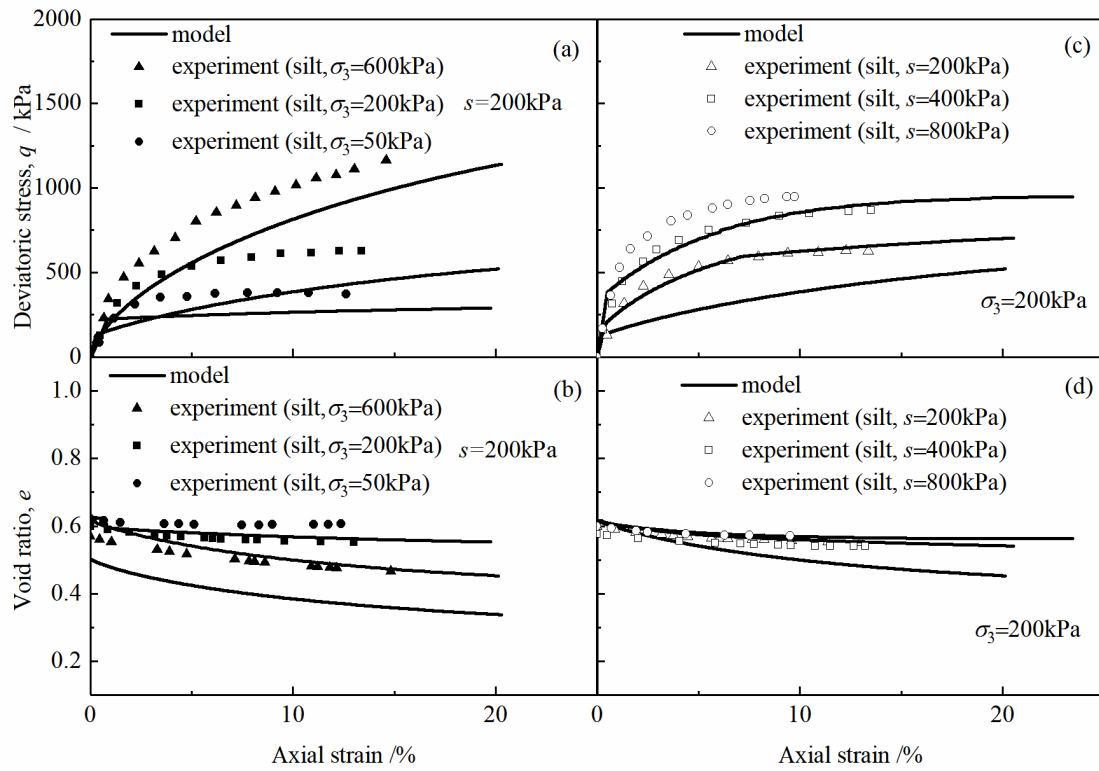


623

624 **Fig. 6.** Comparison between model results and experimental results (Almahbobi

625

2018) for saturated and unsaturated shear: (a/c)  $q$ ; (b/d)  $e$



626

627 **Fig. 7.** Comparison between model results and experimental results on Jossigny silt

628 (Cui and Delage 1996) for shear at constant suction or cell pressure: (a/c)  $q$ ; (b/d)  $e$

629